Geochemical Perspectives Letters

Inferred pyrite growth via the particle attachment pathway in the presence of trace metals

J.M. Domingos[1], E. Runge[1], C. Dreher[2], T.-H. Chiu[2], J. Shuster[3], S. Fischer[3], A. Kappler[2,4], J.-P. Duda[1], J. Xu[5,6], M. Mansor[2,5*]

https://doi.org/10.7185/geochemlet.2318

Abstract

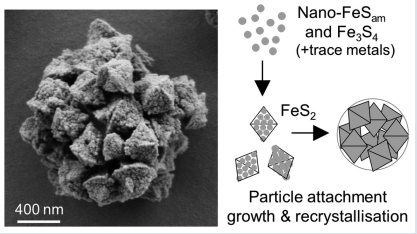

The morphology of pyrite has been used to infer ancient redox states and biogenicity. However, the influence of trace metals on pyrite morphology is poorly understood. Through batch synthesis experiments, we demonstrate that bioessential trace metals (Co, Cu, Mo, Ni, Zn) accelerate pyrite formation. The first precipitate, FeS$_{am}$, transformed to an intermediate greigite phase and to pyrite with increasing time and temperature. Trace metals either facilitated polysulphide formation or precipitated as nanoparticles that can serve as nuclei for pyrite growth, depending on the initial metal concentration. Despite varying precipitation rates, the final pyrite morphologies were unaffected. Various morphologies including tabular precipitates (<150 nm), aggregates resembling microframboids (100–250 nm), octahedral (300–1500 nm) and rose-like particles (1000–3000 nm) were observed. This size–shape particle continuum was interpreted as stages of pyrite growth via particle attachment. This process could be important in explaining variations in the mineral's reactivity (*e.g.*, defects), isotopic and trace metal distributions, and morphologies (*e.g.*, framboids) for applications in paleo-proxies, environmental research and biosignatures.

Received 31 October 2022 | Accepted 20 April 2023 | Published 9 June 2023

Introduction

Pyrite is a widespread mineral that is involved in a variety of biogeochemical processes with implications for interpreting Earth's past, present and future (Huang *et al.*, 2017). Natural pyrite typically adopts either a euhedral or framboidal (raspberry-like) morphology. Euhedral pyrite is proposed to form via slow growth on pre-existing pyrite, while framboids are proposed to form under fast nucleation conditions in close association with Fe sulphide precursors, such as mackinawite (FeS) and greigite (Fe_3S_4) (Raiswell, 1982; Butler and Rickard, 2000). In the geological record, high abundances of framboids have been interpreted as indicators of euxinic conditions in water columns (Wilkin *et al.*, 1996; Rickard, 2019). The striking morphology of framboids and their association with organic matter have led to their interpretation as biosignatures, despite the various reports of framboid synthesis via abiotic pathways (Ohfuji and Rickard, 2005).

The continuum model for pyrite growth (Sawlowicz, 1993) has received increasing support from growing textural, geochemical and isotopic evidence (Lin *et al.*, 2016, 2017; Liu *et al.*, 2022). In this model, pyrite of different morphologies and sizes reflects cyclic growth stages of small euhedral particles aggregating to form framboids that recrystallise over time into a larger euhedral particle. This continuum model mirrors the particle attachment pathway in that mineral growth occurs via aggregation and recrystallisation of smaller particles. This pathway explains defects in crystal structures, distributions of trace metals and isotopes, and unusual particle morphologies in nature (De Yoreo *et al.*, 2015). This pathway has been demonstrated for pyrite synthesised at >100 °C (Hunger and Benning, 2007; Li *et al.*, 2011; Gong *et al.*, 2013), but not at lower temperatures.

Recent studies have investigated how trace metals impact pyrite formation rates (Table S-1). Comparatively, the effects of trace metals on pyrite morphology are under-constrained. Here, we tested the influence of five bioessential trace metals (Co, Cu, Mo, Ni, Zn) on pyrite formation. These bioessential trace metals are common impurities in pyrite and play key roles in Earth's biogeochemical evolution (Robbins *et al.*, 2016). Their effects on pyrite formation need to be constrained in order to disentangle factors that can affect the utility of pyrite morphologies as environmental proxies and biosignatures.

Fe Sulphide Transformation Sequence

Iron sulphides were synthesised in the presence of 3 mM Fe^{2+}, 6 mM Na_2S and 10 mM elemental sulphur (S^0) in 50 mM HEPES buffer (pH 7). Two sets of experiments were performed and

1. Sedimentology & Organic Geochemistry, Center for Applied Geosciences, University of Tuebingen, 72076 Tuebingen, Germany
2. Geomicrobiology, Center for Applied Geosciences, University of Tuebingen, 72076 Tuebingen, Germany
3. Tuebingen Structural Microscopy Core Facility, University of Tuebingen, 72076 Tuebingen, Germany
4. Cluster of Excellence: EXC 2124: Controlling Microbes to Fight Infection, 72076 Tuebingen, Germany
5. NanoGeoBio, Department of Geological Sciences, The University of Texas at El Paso, TX 79968, El Paso, USA
6. School of Molecular Sciences, Arizona State University, AZ 85278, Tempe, USA
* Corresponding author (email: muammar.muammar-bin-mansor@uni-tuebingen.de)

termed *Set-1* (97 % N_2, 3 % H_2 headspace) and *Set-2* (100 % N_2), respectively (details in SI Methods; Table S-2). In both sets, the addition of Na_2S to Fe^{2+} led to the immediate formation of fine black precipitates identified as a disordered mackinawite-like phase (FeS_{am}) based on a single broad reflection with d-spacings of 5.2–5.3 Å via X-ray diffraction (XRD) (Fig. 1a; Table S-3), and characteristic sheet-like aggregate structures under scanning electron microscopy (SEM) (Fig. 2a) (Csákberényi-Malasics *et al.*, 2012).

Despite following the same methods, *Set-1* and *Set-2* experiments demonstrated differences in greigite contents, pyrite formation rates and the extent of pyritisation. In *Set-1* experiments, FeS_{am} transformed to greigite and eventually to pyrite with increasing time (up to 14 days) and temperature (25–80 °C). FeS_{am} was no longer detectable by XRD after 14 days of incubation at 80 °C, but greigite was still not fully transformed to pyrite (Fig. 1a). Comparatively, in *Set-2* experiments, FeS_{am} was completely transformed to pyrite within 3–7 days of incubation at 80 °C, with no greigite detected. Nonetheless, greigite was likely present at low relative abundances because minerals attracted to hand magnets were observed (Table S-3). These magnetic minerals were associated with black coatings around S^0 particles.

Samples containing greigite and pyrite from *Set-1* experiments were analysed using SEM, which revealed morphologies classified into four categories: tabular (<150 nm), spherical aggregates (100–250 nm), octahedral (300–1500 nm) and rose-like particles (1000–3000 nm) (Fig. 2). Treatment with 6 M HCl led to dissolution of the tabular particles, which we interpret as HCl-soluble greigite given its morphological similarity to previous lab-synthesised greigite (Csákberényi-Malasics *et al.*, 2012; Mansor *et al.*, 2019). The other particles (spherical aggregates, octahedra and "roses") were interpreted as pyrite since they did not dissolve in HCl (Voelz *et al.*, 2019). In *Set-2* experiments, where greigite was not detected by XRD, tabular particles were rarely observed whilst other particles were common. Occasionally, acicular particles (100–5000 nm length) were also observed from day 3 onwards and identified via energy dispersive X-ray spectroscopy (EDS) to be rich in Fe and oxygen, suggestive of Fe(III) oxyhydroxides (Fig. S-1).

Overall, *Set-1* and *Set-2* experiments exhibited similar transformation sequences of FeS_{am} to greigite to pyrite with increasing time and temperature, consistent with previous studies (Hunger and Benning, 2007; Mansor and Fantle, 2019). Alternative pathways without a greigite intermediate are possible (see Sanden *et al.*, 2021) but seem unlikely in our experiments. We suggest that the differences in pyrite formation rates (~10 × faster in *Set-1*) are caused by the headspace composition (3 % H_2 vs. pure N_2). The lack of H_2 in *Set-2* experiments likely led to a more oxidising condition, which accelerated pyrite formation, consistent with the detection of trace Fe(III) oxyhydroxides (SI Discussion). Differences in headspace gas composition should be considered for experimental studies on pyrite.

Influence of Trace Metals on Pyrite Formation

Prior to Na_2S addition, trace metals (Co, Cu, Mo, Ni, Zn) were added to *Set-1* and *Set-2* experiments to obtain metal:Fe ratios of $1{:}10^5$ and $1{:}10^2$, respectively, to determine their effects on pyrite formation. These ratios represent the broad range of environments (e.g., low temperature sediments, acid mine drainage, hydrothermal vents) in which natural pyrite can form (Von Damm *et al.*, 1985; Shaw *et al.*, 1990; Allman *et al.*, 2021).

From the *low-metal* setups ($1{:}10^5$ ratio), XRD analysis suggested that all trace metals accelerated pyrite formation after 14 days of incubation at 80 °C. The ratio of pyrite/greigite increased in the following order: *no-metal* < Mo < Ni < Cu < Zn < Co, although it must be noted that the ratios overlap within error (Fig. 1b). We were unable to determine if any accelerating effects occurred in the *high-metal setups* ($1{:}10^2$) given the unexpectedly rapid pyrite formation within *Set-2* experiments. In both experimental sets, stronger magnetism was observed in the presence of Mo compared to other metals.

Trace metals were proposed to influence pyrite formation via either: (1) formation of metal-rich nanoparticles that serve as nuclei, (2) complexation or redox reactions that affect polysulphides reactivity and formation, and S(-II) and Fe(II) oxidation,

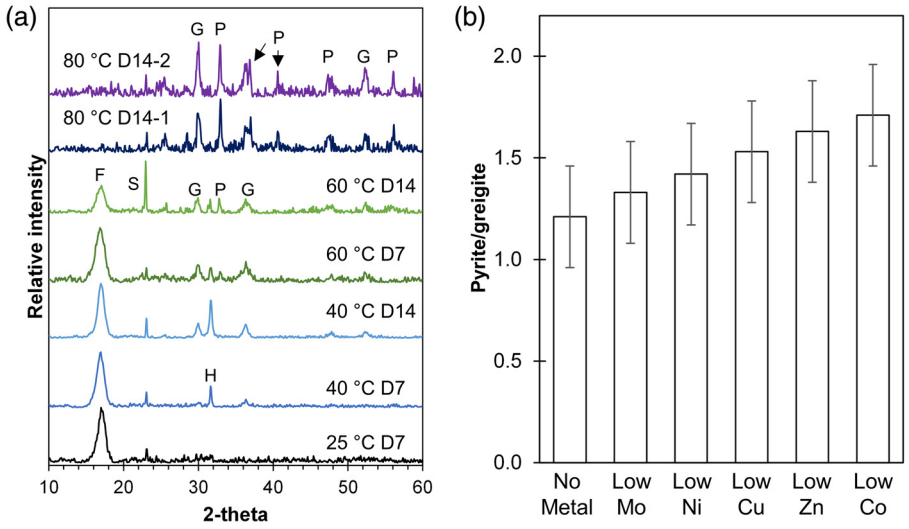

Figure 1 **(a)** XRD patterns showing the progressive transformation from FeS_{am} (F) to greigite (G) and pyrite (P) with increasing temperatures (25, 40, 60 and 80 °C) and time (after 7 and 14 days). Residual sulphur (S) and halite (H) were also detected. Samples from two replicate bottles of experiments at 80 °C after 14 days (80 °C D14-1 or D14-2) indicate high reproducibility. **(b)** Relative intensity of pyrite/greigite signals as determined from thin-film XRD after 14 days of incubation at 80 °C.

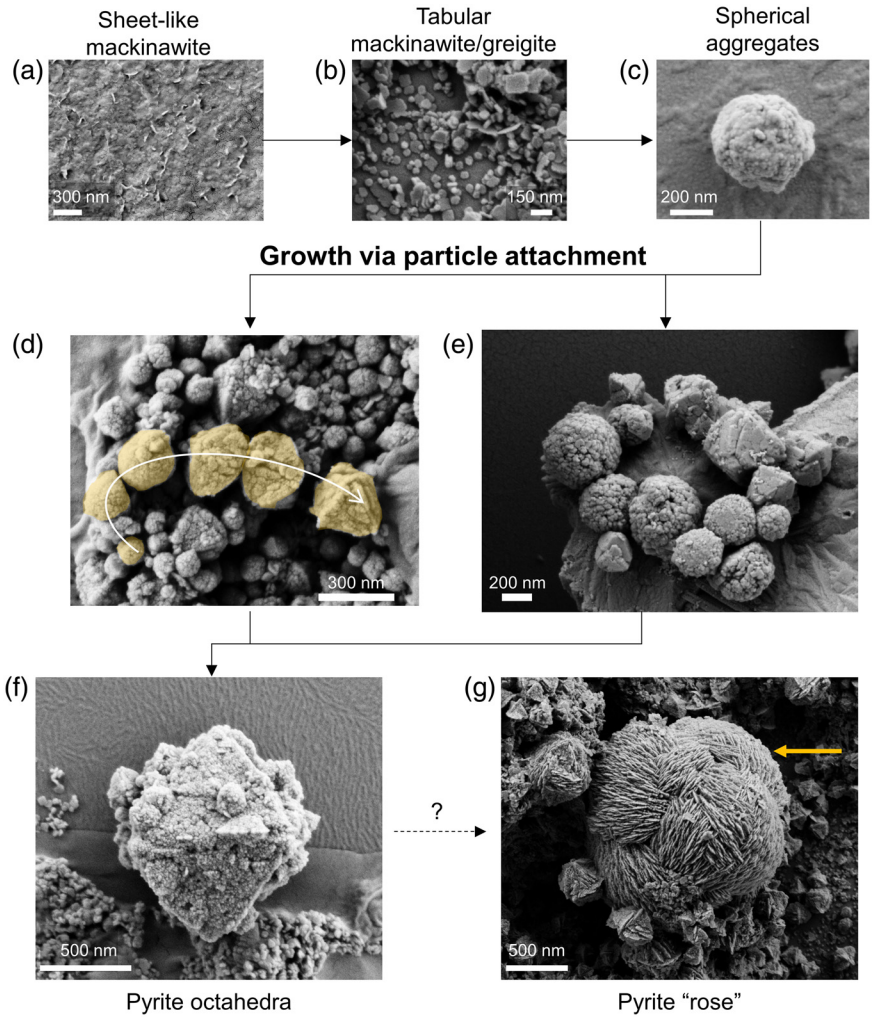

Figure 2 Representative SEM micrographs suggestive of growth via particle attachment. **(a–c)** Transformation of mackinawite to tabular greigite to spherical aggregates of tabular particles. **(d)** The arrow denotes a potential transformation from spherical aggregates to pyrite octahedra. **(e)** Close association between spherical aggregates (microframboids) that are recrystallising to form pyrite octahedra. **(f)** Colloidal pyrite octahedra (centre) with a rough surface and porous structure. **(g)** Micrometre-sized pyrite "rose" (yellow arrow) surrounded by smaller pyrite octahedra. The transformation mechanism may be related to skeletal growth.

or (3) stabilisation of FeS precursors via coprecipitation or adsorption (Table S-1). To test the first two possibilities, we repeated the *no-metal*, *low-metal* (30 nM metals) and *high-metal* (30 μM) setups with the omission of Fe and monitored the formation of nanoparticles and polysulphides at 80 °C.

In the *no-metal* and *low-metal* setups, no precipitates formed and a slight yellow tinge indicative of polysulphides was observed (Fig. 3a). The polysulphide spectra obtained by UV-VIS spectroscopy generally increased in intensity with time with two peaks observed at 275 and 314 nm. At day 1, higher polysulphide peaks were observed in the presence of Co, Cu, Ni and Zn relative to the *no-metal* setup (Fig. 3c–d; S-2). After day 8, however, polysulphides were elevated only in the presence of Co, while the other metals showed no increase or even a slight decrease compared to the *no-metal* setup. High polysulphides with Co correlated with increased pyrite formation rate (Fig. 1b), suggesting that the interaction between this metal and polysulphides may play a role in accelerating pyrite formation.

In the *high-metal* setups, grey or colourless precipitates were formed with all trace metals except for Mo. The yellow polysulphide tinge was evident in the presence of Mo, Cu and Zn but was obscured by the presence of colloidal nanoparticles in the presence of Ni and Co (Fig. 3b). Polysulphide intensities increased with higher trace metal concentrations with the exception of Mo. High Mo concentration induced an additional peak at 470 nm corresponding to tetrathiomolybdate (MoS_4^{2-}) (Erickson and Helz, 2000). The highest polysulphide intensities at day 14 were observed in the presence of high Co concentration, followed by Ni, Cu and Zn (Fig. 3c–d). The amount of polysulphide formed was likely influenced by varying availability of H_2S and S^0 after metal sulphide precipitation. All the metals tested in this study were proposed to form polysulphide complexes (Rickard and Luther, 2006), with Co known to enhance polysulphide conversions in lithium-sulphur batteries (Liu *et al.*, 2021). The interactions between these metals and polysulphides and their impact on biogeochemistry are currently poorly known.

The tentative accelerating effects of Mo and Ni on pyrite formation observed in this study are consistent with previous studies (Table S-1). Mo is also known to promote greigite formation (Mansor and Fantle, 2019; Miller *et al.*, 2020), which could explain the lower pyrite/greigite ratio observed in the presence of Mo compared to other trace metals. In contrast, other studies demonstrated that Co and Ni (Swanner *et al.*, 2019) and Mo

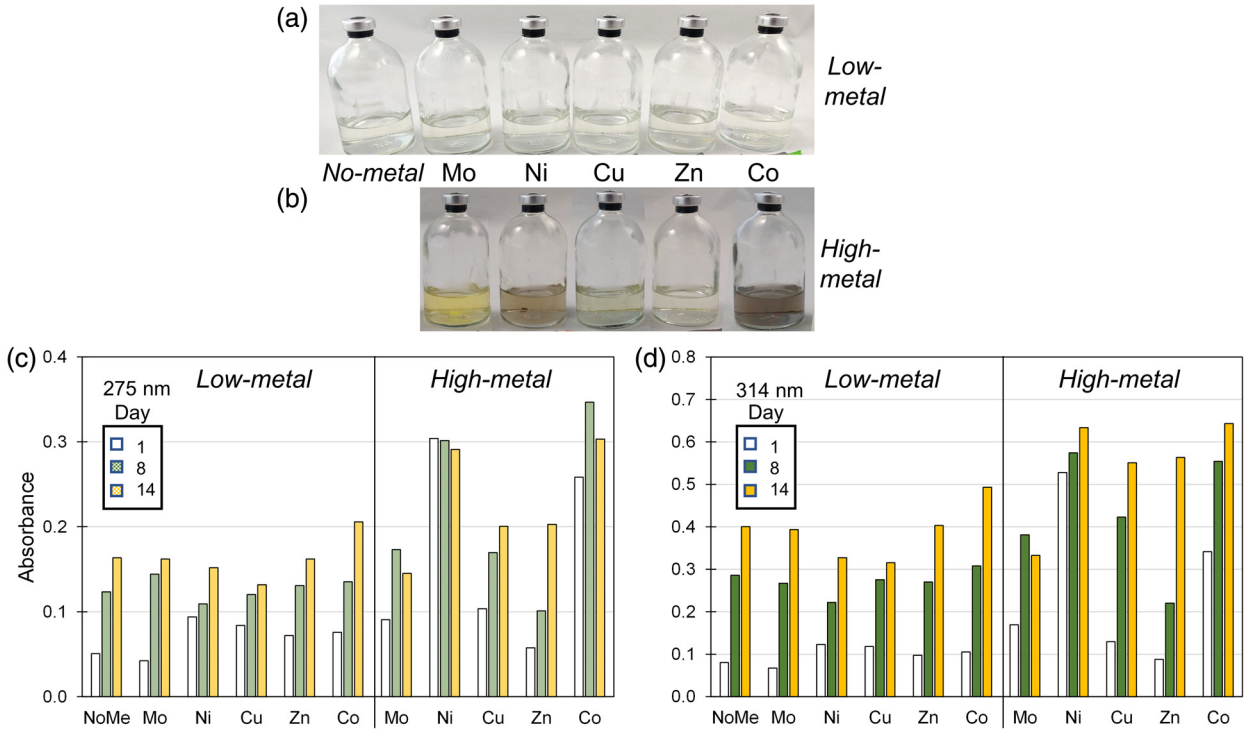

Figure 3 **(a–b)** Pictures of Fe-free setups after 8 days of incubation at 80 °C. Yellow tinge indicates the presence of polysulphides. Precipitates (grey or colourless) are observed in some *high-metal* setups. **(c–d)** Bar charts of the polysulphide peak intensities at (c) 275 nm and (d) 314 nm at Day 1, 8 and 14. Polysulphide intensities increase with time and with higher metal concentrations.

(Baya *et al.*, 2022) inhibited pyrite formation. Differences in metal:Fe ratios and synthesis conditions (*e.g.*, pH and formation pathways) between studies likely led to differences in how specific trace metals affect pyrite formation (SI Discussion). Nevertheless, our results clearly show that trace metals influence polysulphide chemistry and form metal-rich nuclei that may affect pyrite formation.

Despite differences in precipitation rates, the presence of trace metals had little influence on pyrite morphologies (Fig. S-3). Spherical aggregates, octahedral and rose-like particles interpreted as pyrite were present in all samples with no systematic correlation with precipitation rate. Therefore, we conclude that pyrite morphologies were unaffected by trace metal loading. Other factors, such as aging time, S/Fe ratio, organic

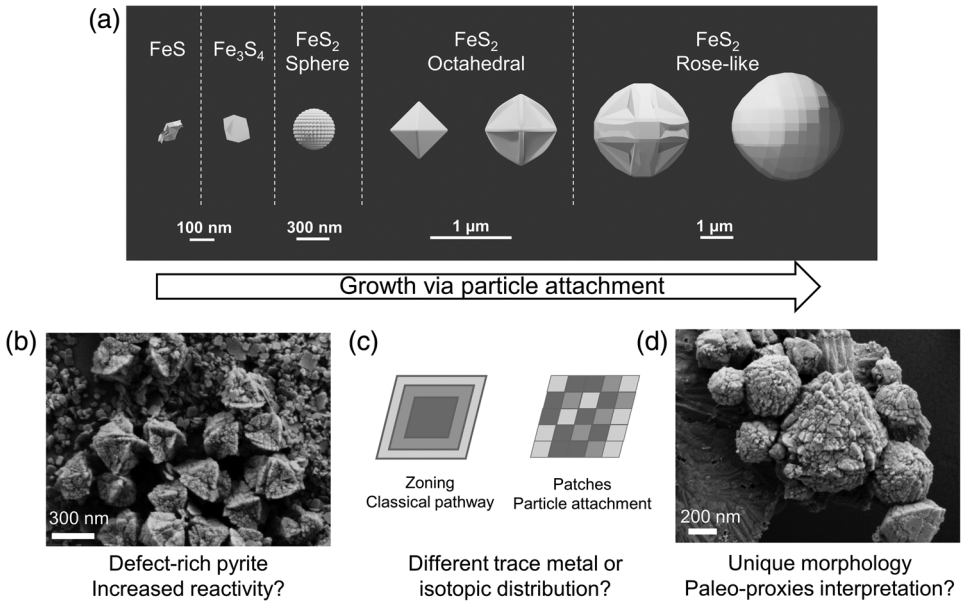

Figure 4 **(a)** Schematic of pyrite formation via particle attachment, showing skeletal growth and twinning between octahedral and rose-like particles (generated in Blender 3.2.2) and **(b–d)** the potential implications to the environment.

matter and biological activities, should be experimentally studied to determine their influence on pyrite morphologies and how these affect subsequent geological interpretations.

Particle Attachment Pathway

Detailed SEM analyses revealed two striking features: (1) particles existed in a continuum of size and shape, and (2) many of the larger particles had rough surface textures that indicate growth via aggregation of smaller particles with varying degrees of recrystallisation, similar in appearance to mesocrystals (Sturm and Cölfen, 2016). Similar surface features have been observed before and interpreted as screw dislocations (Wang and Morse, 1996; Butler and Rickard, 2000). We instead interpret these combined features imaged across multiple experiments as evidence for the particle attachment pathway (Fig. 2, 4) and propose the following transformation sequences. Initially, nanometer-scale FeS_{am} precipitated and transformed to tabular greigite particles (<150 nm). The tabular particles, perhaps in combination with nano-scale FeS_{am} particles, acted as primary units that attached together, forming larger aggregates (<100–250 nm). The aggregates tended to become less rounded and showed signs of recrystallisation towards particles with sharp edges, eventually forming octahedral particles (300–1500 nm). Pyrite containing multiple layers of flat particles and twinned developed into rose-like particles (1000–3000 nm). This morphology was the rarest type observed, and it was more common in *Set-2* compared to *Set-1* experiments. The developmental link between rose-like particles to other smaller particles was less clear. We propose that as particle attachment proceeded on octahedral pyrite, preferential stabilisation of the {111} faces are amplified, leading to a skeletal structure (Fig. 4), similar to those observed previously for ZnS (Xu *et al.*, 2016). The skeletal crystals continue to grow driven by higher attachment rates along the edges (Salas *et al.*, 2021) until they develop into a rose-like structure.

To our knowledge, this is the first time that pyrite formation via particle attachment has been described at <100 °C, leading to micro-framboid formation. *In situ* real-time microscopy observations will be crucial to confirm and describe the exact steps of this pathway. Studies aimed at investigating the subsequent effects on the reactivity and stability of pyrite grains, as well as the distribution of isotopes and trace metals, will help to constrain the potential implications to environmental proxies and biosignature interpretation (Fig. 4).

Acknowledgements

This study was supported by the DFG (SPP 1833, Emmy Noether Programme, 1450/3-2, DU 1450/7-1, JPD; INST 37/1027-1 FUGG, AK) and the German Excellence Strategy of the Federal and State Governments (EXC2124, 390838134; Tuebingen Structural Microscopy Core Facility; AK, MM, SF, JS).

Editor: Liane Benning

Additional Information

Supplementary Information accompanies this letter at https://www.geochemicalperspectivesletters.org/article2318.

Cite this letter as: Domingos, J.M., Runge, E., Dreher, C., Chiu, T.-H., Shuster, J., Fischer, S., Kappler, A., Duda, J.-P., Xu, J., Mansor, M. (2023) Inferred pyrite growth via the particle attachment pathway in the presence of trace metals. *Geochem. Persp. Let.* 26, 14–19. https://doi.org/10.7185/geochemlet.2318

References

Allman, C.J., Gómez-Ortiz, D., Burke, A., Amils, R., Rodriguez, N., Fernández-Remolar, D. (2021) Hydrogeochemical variability of the acidic springs in the Rio Tinto headwaters. *Water* 13, 2861. https://doi.org/10.3390/w13202861

Baya, C., Le Pape, P., Baptiste, B., Menguy, N., Delbes, L., Morand, M., Rouelle, M., Aubry, E., Ona-Nguema, G., Noël, V. and Juillot, F. (2022) A methodological framework to study the behavior and kinetic influence of V, Mn, Co, Ni, Cu, Zn, As, Se and Mo during pyrite formation via the polysulfide pathway at ambient temperature. *Chemical Geology* 613. https://doi.org/10.1016/j.chemgeo.2022.121139

Butler, I.B., Rickard, D. (2000) Framboidal pyrite formation via the oxidation of iron (II) monosulfide by hydrogen sulphide. *Geochimica et Cosmochimica Acta* 64, 2665–2672. https://doi.org/10.1016/S0016-7037(00)00387-2

Csákberényi-Malasics, D., Rodriguez-Blanco, J.D., Kis, V.K., Rečnik, A., Benning, L.G., Pósfai, M. (2012) Structural properties and transformations of precipitated FeS. *Chemical Geology* 294–295, 249–258. https://doi.org/10.1016/j.chemgeo.2011.12.009

De Yoreo, J.J., Gilbert, P.U., Sommerdijk, N.A., Penn, R.L., Whitelam, S., Joester, D., Zhang, H., Rimer, J.D., Navrotsky, A., Banfield, J.F. and Wallace, A.F. (2015) Crystallization by particle attachment in synthetic, biogenic, and geologic environments. *Science* 349, aaa6760. https://doi.org/10.1126/science.aaa6760

Erickson, B.E., Helz, G.R. (2000) Molybdenum(VI) speciation in sulfidic waters: Stability and lability of thiomolybdates. *Geochimica et Cosmochimica Acta* 64, 1149–1158. https://doi.org/10.1016/S0016-7037(99)00423-8

Gong, M., Kirkeminde, A., Ren, S. (2013) Symmetry-defying iron pyrite (FeS_2) nanocrystals through oriented attachment. *Scientific Reports* 3, 1–6. https://doi.org/10.1038/srep02092

Huang, F., Gao, W., Gao, S., Meng, L., Zhang, Z., Yan, Y., Ren, Y., Li, Y., Liu, K., Xing, M. and Wang, Y. (2017) Morphology evolution of nano-micron pyrite: A review. *Journal of Nanoscience and Nanotechnology* 17, 5980–5995. https://doi.org/10.1166/jnn.2017.14430

Hunger, S., Benning, L.G. (2007) Greigite: A true intermediate on the polysulfide pathway to pyrite. *Geochemical Transactions* 8, 1–20. https://doi.org/10.1186/1467-4866-8-1

Li, W., Döblinger, M., Vaneski, A., Rogach, A.L., Jäckel, F., Feldmann, J. (2011) Pyrite nanocrystals: Shape-controlled synthesis and tunable optical properties via reversible self-assembly. *Journal of Materials Chemistry* 21, 17946–17952. https://doi.org/10.1039/c1jm13336e

Lin, Z., Sun, X., Peckmann, J., Lu, Y., Xu, L., Strauss, H., Zhou, H., Gong, J., Lu, H. and Teichert, B.M. (2016) How sulfate-driven anaerobic oxidation of methane affects the sulfur isotopic composition of pyrite: A SIMS study from the South China Sea. *Chemical Geology* 440, 26–41. https://doi.org/10.1016/j.chemgeo.2016.07.007

Lin, Z., Sun, X., Lu, Y., Strauss, H., Xu, L., Gong, J., Teichert, B.M., Lu, R., Lu, H., Sun, W. and Peckmann, J. (2017) The enrichment of heavy iron isotopes in authigenic pyrite as a possible indicator of sulfate-driven anaerobic oxidation of methane: Insights from the South China Sea. *Chemical Geology* 449, 15–29. https://doi.org/10.1016/j.chemgeo.2016.11.032

Liu, K., Huang, F., Gao, S., Zhang, Z., Ren, Y., An, B. (2022) Morphology of framboidal pyrite and its textural evolution: Evidence from the Logatchev area, Mid-Atlantic Ridge. *Ore Geology Reviews* 141. https://doi.org/10.1016/j.oregeorev.2021.104630

Liu, W., Luo, C., Zhang, S., Zhang, B., Ma, J., Wang, X., Liu, W., Li, Z., Yang, Q.H. and Lv, W. (2021) Cobalt-doping of molybdenum disulfide for enhanced catalytic polysulfide conversion in lithium-sulfur batteries. *ACS Nano* 15, 7491–7499. https://doi.org/10.1021/acsnano.1c00896

Mansor, M., Fantle, M.S. (2019) A novel framework for interpreting pyrite-based Fe isotope records of the past. *Geochimica et Cosmochimica Acta* 253, 39–62. https://doi.org/10.1016/j.gca.2019.03.017

Mansor, M., Berti, D., Hochella Jr, M.F., Murayama, M., Xu, J. (2019) Phase, morphology, elemental composition and formation mechanisms of biogenic and abiogenic Fe-Cu-sulfide nanoparticles: A comparative study on their occurrences under anoxic conditions. *American Mineralogist* 104, 703–717. https://doi.org/10.2138/am-2019-6848

Miller, N., Dougherty, M., Du, R., Sauers, T., Yan, C., Pines, J.E., Meyers, K.L., Dang, Y.M., Nagle, E., Ni, Z. and Pungsrisai, T. (2020) Adsorption of tetrathiomolybdate to iron sulfides and its impact on iron sulfide transformations. *ACS Earth and Space Chemistry* 4, 2246–2260. https://doi.org/10.1021/acsearthspacechem.0c00176

Ohfuji, H., Rickard, D. (2005) Experimental syntheses of framboids - A review. *Earth-Science Reviews* 71, 147–170. https://doi.org/10.1016/j.earscirev.2005.02.001

Raiswell, R. (1982) Pyrite texture, isotopic composition and the availability of iron. *American Journal of Science* 282, 1244–1263. https://doi.org/10.2475/ajs.282.8.1244

Rickard, D. (2019) Sedimentary pyrite framboid size-frequency distributions: A meta-analysis. *Palaeogeography, Palaeoclimatology, Palaeoecology* 522, 62–75. https://doi.org/10.1016/j.palaeo.2019.03.010

Rickard, D., Luther, G.W. (2006) Metal sulfide complexes and clusters. *Reviews in Mineralogy and Geochemistry* 61, 421–504. https://doi.org/10.2138/rmg.2006.61.8

Robbins, L.J., Lalonde, S.V., Planavsky, N.J., Partin, C.A., Reinhard, C.T., Kendall, B., Scott, C., Hardisty, D.S., Gill, B.C., Alessi, D.S. and Dupont, C.L. (2016) Trace elements at the intersection of marine biological and geochemical evolution. *Earth-Science Reviews* 163, 323–348. https://doi.org/10.1016/j.earscirev.2016.10.013

Salas, P., Ruprecht, P., Hernández, L., Rabbia, O. (2021) Out-of-sequence skeletal growth causing oscillatory zoning in arc olivines. *Nature Communications* 12. https://doi.org/10.1038/s41467-021-24275-6

Sanden, S.A., Szilagyi, R.K., Li, Y., Kitadai, N., Webb, S.M., Yano, T., Nakamura, R., Hara, M., McGlynn, S.E. (2021) Electrochemically induced metal- vs. ligand-based redox changes in mackinawite: identification of a Fe^{3+}- and polysulfide-containing intermediate. *Dalton Transactions* 50, 11763–11774. https://doi.org/10.1039/D1DT01684A

Sawlowicz, Z. (1993) Pyrite framboids and their development: a new conceptual mechanism. *Geologische Rundschau* 82, 148–156. https://doi.org/10.1007/BF00563277

Shaw, T.J., Gieskes, J.M., Jahnke, R.A. (1990) Early diagenesis in differing depositional environments: The response of transition metals in pore water. *Geochimica et Cosmochimica Acta* 54, 1233–1246. https://doi.org/10.1016/0016-7037(90)90149-F

Sturm, E. V., Cölfen, H. (2016) Mesocrystals: Structural and morphogenetic aspects. *Chemical Society Reviews* 45, 5821–5833. https://doi.org/10.1039/C6CS00208K

Swanner, E.D., Webb, S.M., Kappler, A. (2019) Fate of cobalt and nickel in mackinawite during diagenetic pyrite formation. *American Mineralogist* 104, 917–928. https://doi.org/10.2138/am-2019-6834

Voelz, J.L., Johnson, N.W., Chun, C.L., Arnold, W.A., Penn, R.L. (2019) Quantitative dissolution of environmentally accessible iron residing in iron-rich minerals: A review. *ACS Earth and Space Chemistry* 3, 1371–1392. https://doi.org/10.1021/acsearthspacechem.9b00012

Von Damm, K.L., Edmond, J.M., Grant, B., Measures, C.I., Walden, B., Weiss, R.F. (1985) Chemistry of submarine hydrothermal solutions at 21°N, East Pacific Rise. *Geochimica et Cosmochimica Acta* 49, 2197–2220. https://doi.org/10.1016/0016-7037(85)90222-4

Wang, Q., Morse, J.W. (1996) Pyrite formation under conditions approximating those in anoxic sediments I. Pathway and morphology. *Marine Chemistry* 52, 99–121. https://doi.org/10.1016/0304-4203(95)00082-8

Wilkin, R.T., Barnes, H.L., Brantley, S.L. (1996) The size distribution of framboidal pyrite in modern sediments: An indicator of redox conditions. *Geochimica et Cosmochimica Acta* 60, 3897–3912. https://doi.org/10.1016/0016-7037(96)00209-8

Xu, J., Murayama, M., Roco, C.M., Veeramani, H., Michel, F.M., Rimstidt, J.D., Winkler, C., Hochella, M.F. (2016) Highly-defective nanocrystals of ZnS formed via dissimilatory bacterial sulfate reduction: A comparative study with their abiogenic analogues. *Geochimica et Cosmochimica Acta* 180, 1–14. https://doi.org/10.1016/j.gca.2016.02.007